



Article

# Neovascularization Effects of Carbon Monoxide Releasing Drugs Chemisorbed on *Coscinodiscus* Diatoms Carriers Characterized by Spectromicroscopy Imaging

Joachim Delasoie <sup>1</sup>, Natasa Radakovic <sup>2</sup>, Aleksandar Pavic <sup>2,\*</sup> and Fabio Zobi <sup>1,\*</sup>

<sup>1</sup> Department of Chemistry, Fribourg University, Chemin du Musée 9, 1700 Fribourg, Switzerland; joachim.delasoie@unifr.ch

<sup>2</sup> Institute of Molecular Genetics and Genetic Engineering, University of Belgrade, Vojvode Stepe 444a, 11042 Belgrade, Serbia; radakovicn@imgge.bg.ac.rs

\* Correspondence: sasapavic@imgge.bg.ac.rs (A.P.); fabio.zobi@unifr.ch (F.Z.)

Received: 29 September 2020; Accepted: 19 October 2020; Published: 21 October 2020



**Abstract:** Silica microparticles made of diatomaceous earth have become particularly attractive materials for designing drug delivery systems. In order to investigate the use of natural diatoms as drug scaffolds for carbon monoxide releasing molecules (CORMs), we evaluated the chemisorption of the cis-[Re(CO)<sub>2</sub>Br<sub>4</sub>]<sup>2-</sup> complex (ReCORM-2) and its vitamin B<sub>12</sub> derivative (B<sub>12</sub>-ReCORM-2) on *Coscinodiscus* frustules by 3D FT-IR spectroscopic imaging, and the drugs' neovascularization effects in vivo in the zebrafish (*Danio rerio*) model. By mapping the symmetric Re-C≡O ν(CO) stretching vibration of the CORMs in the 2000 cm<sup>-1</sup> region, we found that the drugs are mostly localized at the girdle band of the diatom frustule. Both ReCORM-2 and B<sub>12</sub>-ReCORM-2 retain their CO-releasing ability when chemisorbed on the diatoms. When applied in vivo at doses ≥25 μM, the molecules markedly reduced intersegmental and subintestinal vessels development in zebrafish, revealing high anti-angiogenic potential. In addition, diatom frustules did not provoke any toxic in vivo response in the zebrafish embryos, including inflammation. Overall, our results indicate that: (1) CORMs chemisorbed on diatom frustules retain their CO-releasing abilities; (2) both CO-releasing molecules show a concentration-dependent effect on the neovascularization in developing zebrafish; (3) silicate frustules are not toxic and could be used as CORMs drug carriers.

**Keywords:** CORM; rhenium; diatoms; zebrafish; neovascularization; angiogenesis

## 1. Introduction

Carbon monoxide releasing molecules (CORMs) are drugs that are examined to explicitly convey carbon monoxide (CO) to unhealthy or aggravated tissues to start and advance remedial impacts at the site of disease. In several mammalian tissues, carbon monoxide mitigates important physiological effects embracing antiproliferative, anti-inflammatory, and anticoagulative responses [1–10]. Metal carbonyl complexes have been dominantly assessed as CORMs. There are currently various models available in the literature, with CORM-2 and CORM-3 (Figure 1) being the best-known complexes of this class of pharmaceutical compounds. The molecules are known to reverse the inhibition of mitochondrial biogenesis [11–15] and prevent doxorubicin-induced cardiac cell death [16,17]. CORM-2 and CORM-3, e.g., exert in vivo a positive effect in doxorubicin (Dox)-induced cardiomyopathy. CORM-2 protects the myocardium from Dox exposure by decreasing apoptosis and oxidative stress, while CORM-3, in a rat model of Dox-induced cardiomyopathy, induces a positive inotropic effect by increasing systolic pressure of the heart [17]. CORMs have also recently been evaluated as anticancer compounds [18],

and their liberated CO plays an important role in vascular functions with concentration-dependent pro-angiogenic [19–23] and anti-angiogenic [24] effects [25]. Our contribution to the field was the introduction of 17-electron Re complexes [26–28] (Figure 1) showing cardioprotective [13] and anticoagulative [6] effects.

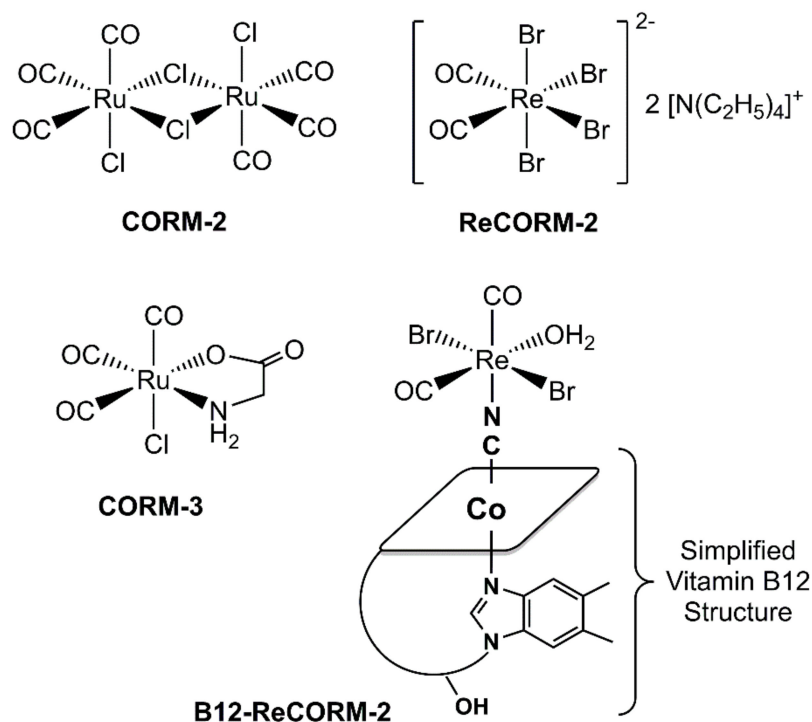


**Figure 1.** Chemical structures of CORM-2, CORM-3, and ReCORM-2 and B<sub>12</sub>-ReCORM-2 (used in this study).

Because of their unique signatures, vibrational spectroscopy is the most commonly used structural technique for the characterization of such chemical systems. Metal carbonyl complexes are recognized for their distinctive infrared (IR) properties. They exhibit energetically segregated vibrations in a segment of the electromagnetic spectrum (characteristically in the 2100–1800  $cm^{-1}$  region) amiable to rapid interpretation. This characteristic has allowed, e.g., for the IR mapping of several metal carbonyl-based drugs in live cells [29–39]. In recent years, macromolecular systems have also begun to be exploited as CORM carriers in an attempt to improve the pharmacokinetic properties of the molecules [40–42]. To date micelles [43,44], magnetic iron oxide particles [45], porous coordination polymers [46], polymer matrices [47–49] and nanoparticles [50–53], have been described. Permeable silica-based materials are especially appealing for drug-delivery applications because of their biocompatibility and degradability, in addition to their thermal and chemical stability. However, their synthesis is expensive, tedious and habitually requires poisonous substances. In 1999, Morse proposed the utilization of natural diatoms as an option in contrast to manufactured silica-based materials for bio-applications [54]. Diatoms are unicellular organisms flourishing in all aquatic and wet environments. These creatures have the remarkable element of being encased inside a cell wall made of hydrated silicon dioxide called a frustule. The hereditarily controlled design of the frustule of these creatures surpasses the current human designing abilities and, because of their abundance, various shapes, and physical-chemical properties, they can be very useful in material chemistry, biology, and medicine. Effective frustule encapsulation has been accounted for several medications [55–60], but the key for the further development of these composite materials is also a thorough comprehension of the drug distribution in the same.

Within the context above, we have decided to functionalize via standard chemisorption techniques *Coscinodiscus* diatoms frustules with the promising CO releasing drug *cis*-[Re(CO)<sub>2</sub>Br<sub>4</sub>]<sup>2-</sup> (ReCORM-2) and B<sub>12</sub>-ReCORM-2 (Figure 1). We studied the compounds' distribution on the frustules via FT-IR

spectromicroscopy imaging (FTIR-SMI) and their release profile. Furthermore, we have for the first time, investigated in vivo the toxicity of the Re-based CORMs and diatoms using the zebrafish (*Danio rerio*) model, as well as the drugs' potential to suppress the neoangiogenesis process in vivo. Overall, our study indicates that CORMs chemisorbed on diatom frustules retain their CO-releasing abilities and that they are rapidly released from the same. We show that 3D FT-IR spectroscopic imaging is a powerful technique to help to elucidate CORM localization and reactivity on silica-based materials and that both CO-releasing molecules show a concentration-dependent effect on the neovascularization in developing zebrafish. This property could be beneficial for their potential therapeutic applications, e.g., the stimulation of wound healing (pro-angiogenic effect) or anticancer effect (anti-angiogenic effect). We hope our study can contribute to the long-term goal of developing functional bio-inspired materials for CORM delivery applications.

## 2. Materials and Methods

### 2.1. Chemicals and Samples Preparation

Chemicals and solvents were purchased from standard sources.  $\text{NaReO}_4$  and vitamin B12 were purchased from Sigma-Aldrich (Buchs, Switzerland). The synthesis of the  $[\text{Et}_4\text{N}]_2 \text{cis}-[(\text{CO})_2\text{ReBr}_4]$  salt (ReCORM-2) and  $\text{B}_{12}$ -ReCORM-2 was performed according to the literature [27,61]. Glycerol and sodium dithionite ( $\text{Na}_2\text{S}_2\text{O}_4$ ) were purchased from Reactolab SA (Servion, Switzerland) and Fisher Scientific AG (Reinach, Switzerland), respectively. Diatom samples for FTIR spectromicroscopy imaging and biological studies were prepared by using *Coscinodiscus* and *Aulacoseira* diatoms, respectively. Diatomaceous earth, in the form of Celatom<sup>®</sup> Fw-14, was obtained from Applied Minerals Ltd. (Burton, Staffordshire, UK). This earth was used to isolate *Aulacoseira* frustules of average 10 and 23  $\mu\text{m}$  size, for toxicity studies, according to a published procedure [62]. The silicon skeleton of diatoms is a major component of commercially available filtering agents as, e.g., diatomaceous earth or Celite. *Coscinodiscus* (CF) valves were isolated from Celite 450 (delivered by Sigma-Aldrich, Buchs, Switzerland) according to the following procedure: 1 g of Celite was suspended in 10 mL of 1M HCl (Honey-well Research chemicals, Bucharest, Romania) and stirred vigorously for 15 h at room temperature. The slurry was then filtered and washed with water. The mixture was poured on metallic mesh sieves (300/150/63  $\mu\text{m}$ ) for sequential filtration and washed ten times with 30 mL of pure water. The fraction accumulated on the 63  $\mu\text{m}$  mesh was collected and dried. Frustules chemisorption of ReCORM-2 and  $\text{B}_{12}$ -ReCORM-2 on *Coscinodiscus* (CF) was achieved by the method described by Vasani et al. [63]. Frustules were then filtered and washed several times with dry  $\text{CH}_2\text{Cl}_2$  and  $\text{CH}_3\text{CN}$  (Sigma-Aldrich, Buchs, Switzerland) until washings were clear. Solutions of ReCORM-2 and  $\text{B}_{12}$ -ReCORM-2 are red in color, but after filtration and washing, the visual appearance of the frustules remained that of an off-grey slightly pink material. The loading degrees for ReCORM-2 and  $\text{B}_{12}$ -ReCORM-2 were calculated as  $8.0 \pm 2.2$  and  $6.8 \pm 1.7$  wt% [63,64]. These loading percentages are in the normal loading range detailed for other molecules [55,64–66]. Isolated *Coscinodiscus* frustules treated by this method are referred to as CF-1 (for ReCORM-2) and CF-12 (for  $\text{B}_{12}$ -ReCORM-2).

### 2.2. Characterization

UV-Vis and IR spectra were recorded using a Jasco V730 spectrophotometer (Echallens, Switzerland) and a Perkin Elmer FTIR Frontier Serie 99155 (Schwerzenbach, Switzerland) equipped with a PIKE TECHNOLOGIES GladiATR™ (OPUS 7.5 software) respectively. Measurements of inductively coupled plasma with optical emission spectroscopy (ICP-OES) were executed with a Perkin Elmer Optima 7000 DV (Schwerzenbach, Switzerland). FTIR spectromicroscopy imaging was performed with a PerkinElmer Spotlight 400 FT-IR imaging system (Schwerzenbach, Switzerland) equipped with a linear array detector that incorporates high-quality pure mercury cadmium telluride (MCT) arranged as 16 gold-wired infrared detector elements. Each image was collected with a spectral resolution of  $2 \text{ cm}^{-1}$  averaged over 32 scans for a  $200 \times 200 \mu\text{m}$  area. This gave  $32 \times 32$  pixel image areas

with a  $6.25 \times 6.25 \mu\text{m}$  pixel resolution. Chemical maps for each specific wavenumber were automatically generated by the SpectrumIMAGE software R 1.8.0.0411 as average contour areas plotted by taking each maximum pixel intensity. In order to acquire chemical maps of CF-1 and CF-12 samples, frustules were allowed to settle in a thin film of paratone oil on round  $\text{CaF}_2$  windows (2 cm in diameter; 2 mm thickness) housed in a custom made holder. All images were recorded in transmission mode.

### 2.3. Drug Release and CO-Releasing Properties of CF-1 and -12

In order to evaluate if CF-1 and CF-12 retained CO-releasing properties, the material was tested via the standard myoglobin assay [67]. In these experiments, a few  $\mu\text{g}$  of CF-1 or CF-12 (typically 250–500  $\mu\text{g}$ ) were suspended in a newly prepared buffered solution (3 mL) of horse skeletal myoglobin (Mb, Sigma-Aldrich, Buchs, Switzerland), reduced under a nitrogen atmosphere with excess  $\text{Na}_2\text{S}_2\text{O}_4$  at 25 °C and at pH 7.4. The rapid conversion of Mb to carboxymyoglobin (Mb-CO) was then followed by monitoring the spectroscopic changes in the absorption spectra of the Q band region (500–600 nm) of the protein. After the reaction was complete, CFs were once again filtered and imaged by FTIR spectromicroscopy, as described in Section 2.2. The drug release profiles were considered over periods of 8 h. For each test, 2 to 5 mg of CF-1 and CF-12 was weighed and added in 2 mL Eppendorfs. The experiment was started by adding 2 mL of solvent (PBS buffer, pH 7.4). The concentrations of 100  $\mu\text{l}$  samples of ReCORM-2 (from CF-1) and for  $\text{B}_{12}$ -ReCORM-2 (from CF-12) were measured for each time point by ICP-OES. The cumulative drug releases were calculated based on the Re content of the samples, and the results plotted with the Origin 7.5 program. The cumulative values were calculated from a linear regression obtained with six different concentration standards in the analysis range (from 1 to 35  $\mu\text{g mL}^{-1}$ ,  $R^2 = 0.9855$ ).

### 2.4. In Vivo Toxicity Assessment and Anti-Angiogenic Activity Evaluation

Toxicity evaluation of ReCORM-2 and  $\text{B}_{12}$ -ReCORM-2,  $\text{NaReO}_4$  (sodium perrhenate, CO-free water metabolite of CORMS) [27], vitamin  $\text{B}_{12}$ , and diatoms (13 and 20  $\mu\text{m}$  in diameter) was carried out in the zebrafish (*Danio rerio*) model as previously described [68]. Assessment of lethality and developmental toxicity of the organisms was evaluated at different concentrations of the tested compounds (25, 50, 100, 150, and 250  $\mu\text{M}$  for CO-releasing molecules, vitamin  $\text{B}_{12}$  and  $\text{NaReO}_4$ , and 50, 100, and 200  $\mu\text{g/mL}$  of *Aulacoseira* diatoms, see Supplementary Materials, Table S1). The angiogenesis inhibitory activity of the rhenium CO-releasing molecules was examined in transgenic zebrafish *Tg(fli1:EGFP)* embryos with EGFP-labelled endothelial cells, according to a previously published procedure [69].

### 2.5. Immunotoxicity Assessment

Myelotoxicity (neutropenia and inflammation) of silicate frustules was addressed in the transgenic *Tg(mpx:GFP)* zebrafish embryos expressing green fluorescent protein (GFP) in neutrophils [70], as previously described [69,71]. This enabled us to directly visualize the effect of applied treatments on the neutrophils occurrence, chemotaxis, and accumulation within inflamed tissues and inner organs. Embryos of *Tg(mpx:GFP)* zebrafish were kindly provided by Dr. Ana Cvejic (Wellcome Trust Sanger Institute, Cambridge, UK) and raised in our zebrafish facility to the adult stage under previously described life conditions [68]. At the 6 h post-fertilization (hpf) stage, embryos were exposed to various concentrations of diatoms (50, 100, and 200  $\mu\text{g/mL}$ ) and incubated at 28 °C by 120 hpf. At 120 hpf, embryos were imaged for the neutrophils occurrence under a fluorescence microscope (Olympus BX51, Applied Imaging Corp., San Jose, CA, USA). The Neutrophil's occurrence (according to fluorescence intensity) was determined using the ImageJ 1.50i program (National Institutes of Health, NIH, public domain software). The experiment was performed three times using 10 embryos for each concentration.

### 3. Results and Discussion

#### 3.1. IR Spectra and Chemical Images of Materials

The average solid-state IR spectra of CF, CF-1, and CF-12 are shown in Figure 2. Isolated CF's show characteristic absorption peaks of silicon dioxide with the asymmetric  $\nu(\text{Si-O-Si})$  mode being predominant at  $1100\text{ cm}^{-1}$ . In addition to the characteristic silica signature, after chemisorption of ReCORM-2 and B<sub>12</sub>-ReCORM-2, the IR spectra of CF-1 (red spectrum in Figure 2) and CF-12 (blue spectrum in Figure 2) show respectively weak absorptions at  $1970$  and  $1785\text{ cm}^{-1}$ , and  $2000$  and  $1860\text{ cm}^{-1}$ . These are assigned respectively to the symmetric and asymmetric Re-C≡O  $\nu(\text{CO})$  stretching modes of chemisorbed ReCORMs. It should be noted that following chemisorption of ReCORM-2, CF-1 also showed weak Si-O-Si overtone modes around  $2000$  and  $1870\text{ cm}^{-1}$  assigned to hydrated silicon dioxide [72] and two peaks centered at  $1460$  and  $1400\text{ cm}^{-1}$ . These latter peaks are assigned to a combination of  $\delta(\text{CH}_3)$  and  $\delta(\text{CH}_2)$  vibrations either due to residual organic solvents or the to the Et<sub>4</sub>N<sup>+</sup> counter ion of *cis*-[Re(CO)<sub>2</sub>Br<sub>4</sub>]<sup>2-</sup>. In the case of CF-12 the Si-O-Si overtones are hidden under the Re-C≡O  $\nu(\text{CO})$  stretching modes.

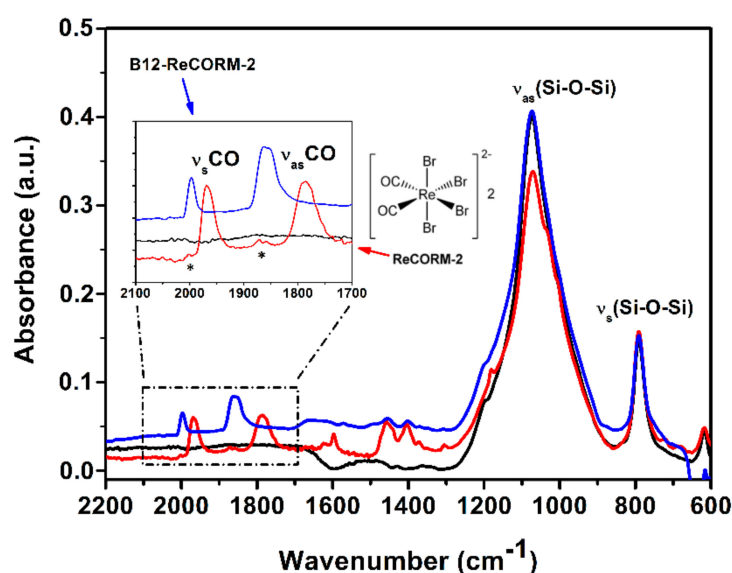


**Figure 2.** Solid-state IR spectra ( $2200\text{--}600\text{ cm}^{-1}$  range) of untreated *Coscinodiscus* frustules (CF, black), ReCORM-2 (CF-1, red trace) and B<sub>12</sub>-ReCORM-2 (CF-12, blue trace) treated *Coscinodiscus* frustules. Insert shows magnified  $2100\text{--}1700\text{ cm}^{-1}$  region. Asterisks (\*) in the insert indicate hydrated silicon dioxide Si-O-Si overtone modes;  $\nu_{\text{s}}\text{CO}$  and  $\nu_{\text{as}}\text{CO}$  indicate respectively the symmetric and asymmetric stretching Re-CO bands of the molecules.

Figure 3 shows optical and MCT detector generated chemical images of single CF-1 and CF-12 valves, which were isolated following chemisorption of *Coscinodiscus* frustules treated with solutions of the CO releasing molecules ReCORM-2 and B<sub>12</sub>-ReCORM-2 [63]. The chemical maps of the selected vibrations show the following features. In both cases, the asymmetric  $\nu(\text{Si-O-Si})$  band at  $1100\text{ cm}^{-1}$  shows the highest intensity in the central region of the diatom valve. The intensity of the  $\nu(\text{Si-O-Si})$  mode slopes to lower values radiating away from the centre to the outer rim of the diatom, known as the girdle band. In the 3D surface representations of the chemical maps (Figure 3E) the roughness of the valve surface, composed of pores of ca.  $0.5\text{ }\mu\text{m}$  in diameter, can be somewhat appreciated. The symmetric and asymmetric Re-C≡O  $\nu(\text{CO})$  stretching modes of chemisorbed ReCORM-2 and B<sub>12</sub>-ReCORM-2, show the highest intensity in the girdle band. This is most evident in the 3D surface representations (Figure 3F) of the symmetric  $\nu(\text{CO})$  vibrations. Depending on the CORM used, the broad symmetric  $\nu(\text{CO})$  mode is found centered at  $2010$  and  $1996\text{ cm}^{-1}$  for CF-12 and CF-1, respectively. The shift is fully consistent with the assignment. In B<sub>12</sub>-ReCORM-2, two of the coordinated Br<sup>-</sup> ions are substituted by

the cyanide group of vitamin B<sub>12</sub> and a solvent molecule [27]. On the basis of both theoretical [73,74] and previous experimental evidence [61,75], we demonstrated that by substituting  $\pi$ -basic ligands (such as Br<sup>-</sup>) with  $\sigma$ -donor or  $\pi$ -acidic ligands (such as CH<sub>3</sub>CN) the symmetric  $\nu(\text{CO})$  stretching frequency of  $[\text{M}(\text{CO})_x\text{L}_{6-x}]^n$  complexes shifts to higher wavenumbers. The apparent discrepancy in the position of the symmetric Re-C $\equiv$ O  $\nu(\text{CO})$  stretching in CF-1 and CF-12, with respect to the solid-state IR (Figure 2), is due to the fact that MCT images were recorded with frustules immersed in a film of paratone oil on round CaF<sub>2</sub> windows.

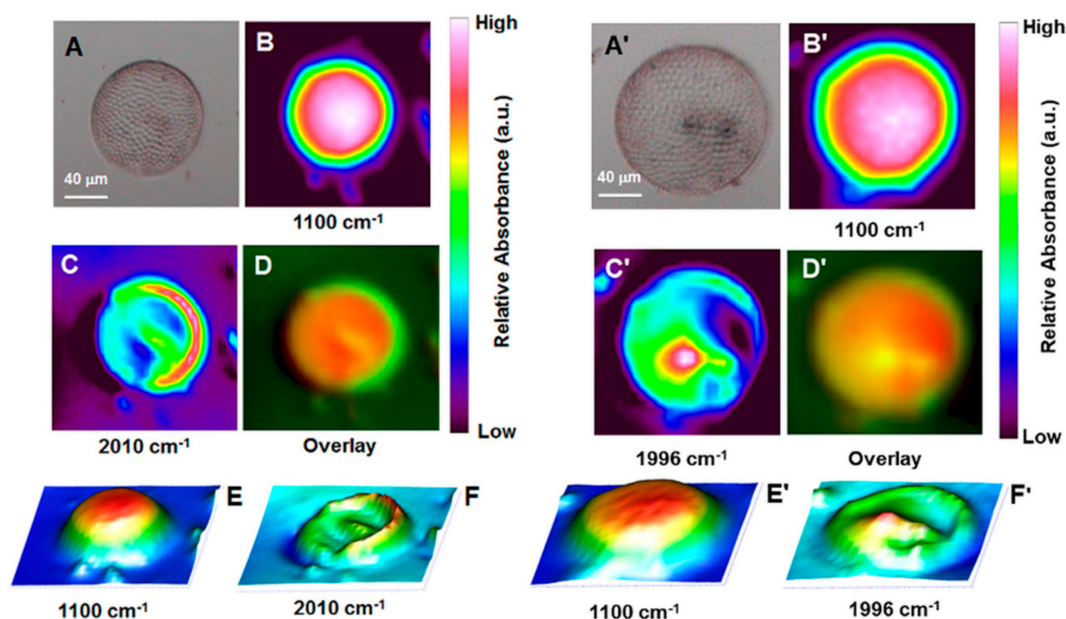


**Figure 3.** MCT detector generated chemical images of single *Coscinodiscus* valves exposed to CH<sub>3</sub>OH solutions of the CO releasing drugs B<sub>12</sub>-ReCORM-2 (left) and ReCORM-2 (right). (A) and (A'): Optical image of single *Coscinodiscus* valve. (B) and (B'): chemical mapping of the Si-O-Si stretching vibration at 1100 cm<sup>-1</sup>. (C) and (C'): chemical mapping of the symmetric C $\equiv$ O stretching mode of B<sub>12</sub>-ReCORM-2 at 2010 (left) and ReCORM-2 at 1996 (right) cm<sup>-1</sup> respectively. (D) and (D'): overlay of (B) and (C), and (B') and (C') respectively. (E) and (E'): 3D surface representations of chemical maps shown in (B) and (B') respectively. (F) and (F'): 3D surface representations of chemical maps shown in (C) and (C') respectively. Images were recorded with frustules allowed to settle in a thin film of paratone oil on round CaF<sub>2</sub> windows (2 cm in diameter; 2 mm thickness).

### 3.2. CO Release, Drug Release, and Chemical Images of Loaded CF's

In order to further corroborate the presence of chemisorbed CORMs on CF and to evaluate if the same retained their CO-releasing ability, CF-1 and CF-12 were suspended in a newly prepared buffered solution of horse skeletal myoglobin (Mb) reduced under a nitrogen atmosphere with excess Na<sub>2</sub>S<sub>2</sub>O<sub>4</sub> at 25 °C and at pH 7.4. As mentioned in Section 2.3., this test (known as the myoglobin assay) is the standard technique to assess the ability of molecules to release CO. It is grounded on the spectroscopic evaluation of the conversion of Mb to carboxymyoglobin (Mb-CO) as evidenced by the change in the absorption spectrum of the Q band region (500–600 nm) of the protein [67]. Figure 4 (top left spectrum) shows the UV-visible spectrum of reduced Mb in the presence of CF and CF-12. As evident from the spectra, i.e., the split of the single Q band absorption of Mb at 555 nm to the two peaks of Mb-CO at 540 and 576 nm, only CF-12 was able to induce the spectroscopic change associated with CO-binding to the protein. This assay confirmed the presence of B<sub>12</sub>-ReCORM-2 in the material and that the same is still able to release CO. Similar results were obtained, under the same conditions, if CF-1 was assessed.

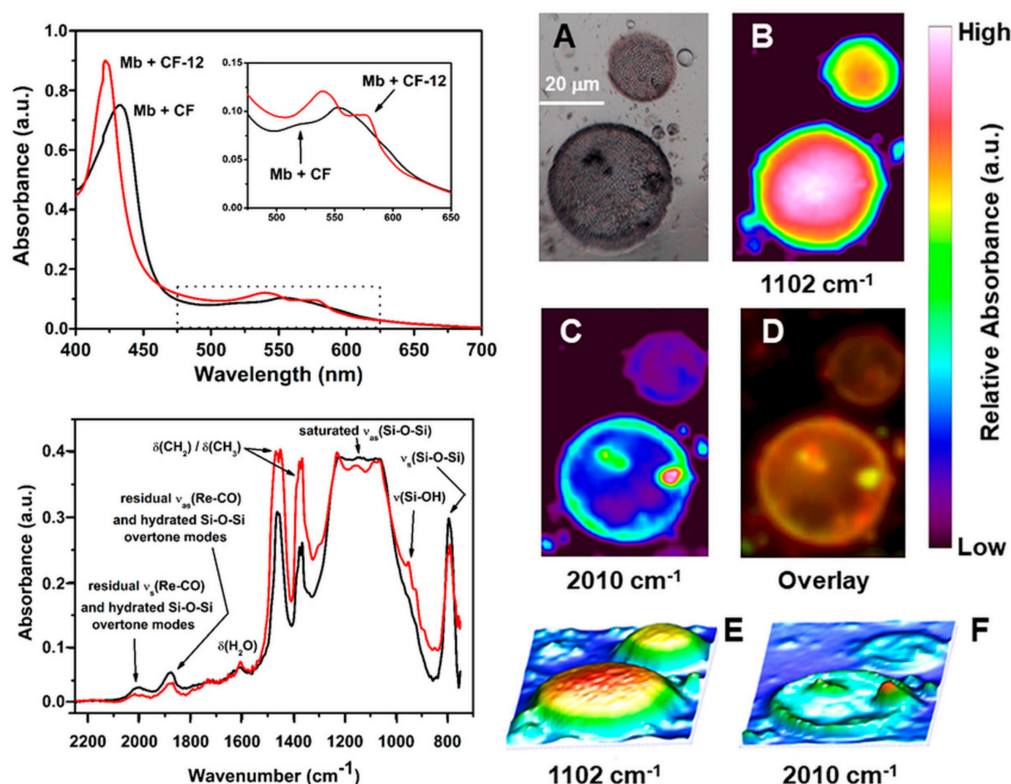


**Figure 4.** Top left: UV-visible spectra of reduced Mb in the presence of CF and CF-12. Insert shows the splitting of the protein Q band (red line) characteristic of carboxymyoglobin (Mb-CO). Bottom Left: IR spectra (2200–700 cm<sup>-1</sup> range) of isolated CF-12 before (black) and after (red) exposure to a buffered solution of reduced Mb. The tentative assignment of major peaks are based on reference [72]. Right: MCT detector generated chemical images of single CF-12 valves exposed to a buffered aqueous solution of reduced myoglobin. (A): Optical image; (B): chemical mapping of the Si-O-Si stretching vibration at 1100 cm<sup>-1</sup>; (C): chemical mapping of the residual symmetric C≡O stretching mode of B<sub>12</sub>-ReCORM-2 at 2010 cm<sup>-1</sup>; (D): overlay of (B) and (C); (E) and (F): 3D surface representations of chemical maps shown in (B) and (C), respectively.

After exposure to the Mb solution, CF-12 was recovered and analyzed once again by FTIR-SMI, in order to evaluate changes in its IR spectrum. A comparison of the average FTIR spectromicroscopy spectra of CF-12 before and after reaction with Mb is given in Figure 4 (bottom left spectrum). There are two fundamental changes in the spectrum. First, the relative intensity of the two weak absorptions in the 2000 and 1880 cm<sup>-1</sup> region decreased after the reaction of CF-12 with Mb. This is consistent with the release of the drug and/or loss of CO by B<sub>12</sub>-ReCORM-2, resulting in a lower relative concentration of its symmetric and asymmetric Re-C≡O ν(CO) stretching modes. Furthermore, there appears to be an increase in intensity of the 952 cm<sup>-1</sup> band (see red spectrum). This vibration has been associated to the stretching mode of vicinal silanols (Si-OH) resulting from an increase of surface concentration of the species following surface hydration [72]. This assignment is fully consistent with CF-12 being exposed to an aqueous solution of Mb. In the same region, however, the frequency of stretching Re = O mode is also reported [76]. As mentioned above, a Re = O species (in the form of perrhenate, ReO<sub>4</sub><sup>-</sup>) is the final product in the aerobic decomposition of the ReCORMs following CO release [27]. We doubt, however, that this band can be assigned to ReO<sub>4</sub><sup>-</sup> given the high solubility of the ion in water.

To evaluate the relative distribution of the above-mentioned vibration, FTIR-SMI maps of Mb-exposed CF-12 were recorded. Figure 4 (right) shows optical and MCT detector generated chemical images acquired in this experiment. The chemical maps of the selected vibrations show the following features. Consistently with images reported in Figure 3 the asymmetric ν(Si-O-Si) band shows the highest intensity

in the central region of the diatom valve and lower intensity on the girdle band. Once again, the roughness of the valve surface can be fully appreciated in the 3D surface representations of the chemical map (Figure 4E). The residual intensity of the weak  $2010\text{ cm}^{-1}$  absorption is highest in the girdle band. This is most evident in the 3D surface representations (Figure 4F) of the vibration. We note once again here that these vibrations also contain the Si-O-Si overtone modes. Thus the observed vibrations in hydrated CF-12 are most likely be due to an overlap of both residual  $\nu(\text{CO})$  Re-C $\equiv$ O stretching vibrations and Si-O-Si overtone modes.

Having established that following chemisorption of ReCORM-2 and B<sub>12</sub>-ReCORM-2 on *Coscinodiscus* frustules the molecules retain their CO-releasing ability, we finally studied CF-1 and CF-12 drug release profiles. The addition of PBS buffer to solid samples of CF-1 and CF-12 initiated drug release, which was monitored by ICP-OES (Re content). As shown in Figure 5, after 1 h of incubation ca. 90% of the drug contents were released from the frustules. The release occurred very rapidly, in particular for ReCORM-2, and was steadily sustained afterward. Examination of the relative profiles of drug discharge indicates that, within experimental error, ReCORM-2 is more rapidly released than B<sub>12</sub>-ReCORM-2 in the first 20 min of incubation, but then similar concentrations of Re metal are measured afterward.

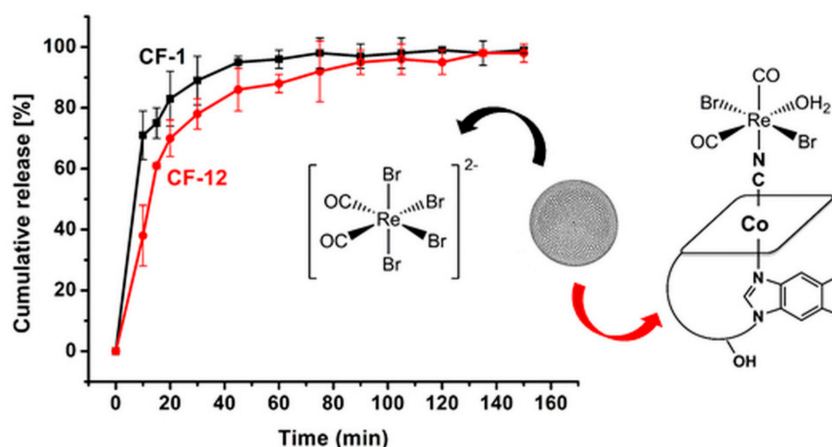


**Figure 5.** Cumulative [%] of Re metal released in PBS buffer, pH 7.4, by CF-1 (black line) and CF-12. The cumulative [%] of Re metal in solution is taken as a measure of drug release.

### 3.3. Assessment of Biological Activities of B<sub>12</sub>-ReCORM-2 and Re-CORM-2 Molecules

The toxicity profile of B<sub>12</sub>-ReCORM-2 and Re-CORM-2 molecules was addressed in vivo using zebrafish embryos, a creature model generally utilized in the current preclinical medication improvement pipeline. Due to their remarkable genetic, physiological, and immunological resemblance to human beings, and high response correspondence to drugs, zebrafish has risen as a flexible biotechnological stage for the toxicity and bioactivity evaluation of chemically synthesized molecules, streamlining the way to preclinical trials and lessening the failure at advanced phases of experimentation and testing [77,78]. To date, the toxicological profile of the rhenium-based CO-releasing molecules has remained unexplored in vivo.

Herein, the toxicity assays were initiated from the 6 h post-fertilization (hpf) stage, when embryos are highly sensitive to applied xenobiotics. The results obtained after 120-h treatment have revealed that both types of molecules were safe at the doses  $<150\ \mu\text{M}$ , while at higher doses, B<sub>12</sub>-ReCORM-2 was more toxic than Re-CORM-2. On the other side, NaReO<sub>4</sub>, the CO-free water metabolite of the CORMs, did not provoke any adverse toxic effect in the treated animals by 120 hpf. Interestingly, see Figure 6 and Table S1 in Supplementary Materials, none of the CORMs provoked the appearance of teratogenic malformations at any applied dose, nor had adverse effects on embryos hatching. This suggests that mortality caused at higher CORMs doses ( $\geq 150\ \mu\text{M}$ ) could be due to the liberated CO, which could diffuse into embryos via the chorion pores and might interfere with the oxygen exchange within the



embryo tissues [79]. In a previous study, Song et al., investigating CORM-3, have found dose-dependent mortality, cardiotoxicity, and inhibitory effect on the embryos hatching, suggesting that CO-mediated inhibition of embryos hatching might play a critical role in the embryo's survival [79]. To address whether the chorion acted as a protective barrier limiting Re-CORM-2 and B<sub>12</sub>-ReCORM-2 passage to embryos, we mechanically removed the chorion at 20 hpf (earlier removal is not safe). B<sub>12</sub>-ReCORM-2 and Re-CORM-2 were then applied onwards at a doses ranging from 50 to 250  $\mu$ M. Data recorded by 120 hpf showed no difference in the survival rates between the groups of embryos with and without chorion, nor any adverse effect of the CO-releasing molecules at the highest applied dose of 250  $\mu$ M (mortality rate of 10% compared to that in the control group). Taken together, the data suggest that the chorion had no effect on embryos survival and that embryos' death (Figure 6) is likely due to embryos' sensitivity at the early developmental stage to CO-releasing molecules. In line with this assumption is the fact that treated embryos died by 48 hpf (data not shown).

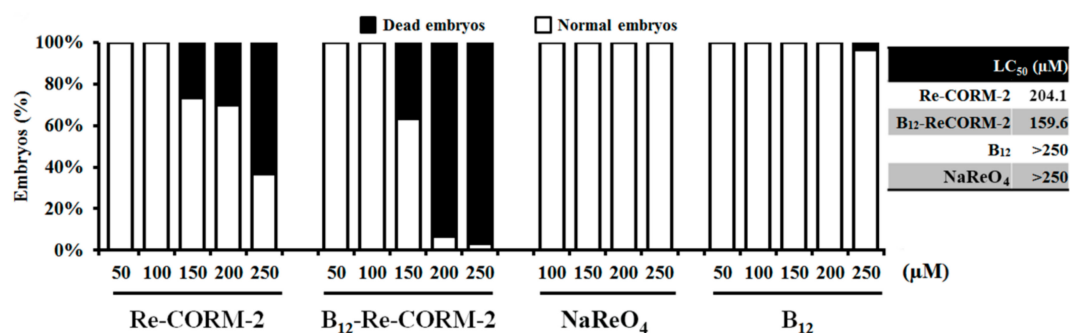


**Figure 6.** Toxicity evaluation of ReCORM-2, B<sub>12</sub>-ReCORM-2, NaReO<sub>4</sub>, and vitamin B<sub>12</sub> addressed in the zebrafish (*Danio rerio*) embryos exposed to different doses in a period from 6 hpf to 120 hpf.

Stimulated by the observation of the reduced circulation in some embryos treated with B<sub>12</sub>-ReCORM-2 at doses  $\geq$ 50  $\mu$ M, we explored both B<sub>12</sub>-ReCORM-2 and ReCORM-2 for the possibility of inhibiting angiogenesis. Neo-angiogenesis (new vessels formation) represents a crucial process for cancer development, intrusion, and metastasis [80], therefore, inhibiting tumor vascularization is a recognized clinical approach for solid malignancies therapy, which, in combination with cytotoxic drugs, could greatly increase the anticancer effectiveness of medications [81].

Suppression of angiogenesis was studied using transgenic zebrafish *Tg(fli1:EGFP)* embryos. In this transgenic line, endothelial cells expressing EGFP can be directly observed by fluorescence microscopy, enabling the detection of the anti-angiogenic drugs without adverse toxic effects. The tested Re-CORM-2 molecules were applied to 6-hpf embryos at a maximum dose of 100  $\mu$ M (corresponding to the highest safety dose of B<sub>12</sub>-ReCORM-2, Figure 7) and inspected at 48 hpf and 72 hpf for the intersegmental vessels (ISVs) and subintestinal vessels (SIVs) development (ISV angiogenesis precedes SIV angiogenesis), respectively. The anti-angiogenic phenotype was characterized by the decreased number/length of SIVs and/or ISVs along the whole body. While in untreated embryos, 28–30 ISVs and 6–9 arcades in the SIV basket-like structure were present, the embryos treated with both molecules at doses  $\geq$ 25  $\mu$ M had markedly reduced the number of both ISVs and SIVs vessels. In the experiment, B<sub>12</sub>-ReCORM-2 demonstrated higher anti-angiogenic potential than ReCORM-2, particularly on the SIVs development ( $p > 0.001$ , Figure 7). We note that the majority of ISV vessels were affected at 100  $\mu$ M of B<sub>12</sub>-ReCORM-2 (see Supplementary Materials Figure S1), showing a markedly decreased EGFP expression as an indication of the cells viability loss, without affecting other inner organs' functioning and development. None of the tested molecules inhibited angiogenesis at the doses below 25  $\mu$ M, according to the fluorescence intensity of the vessels in hematopoietic tissues. Although vessel fluorescence in these areas was not measured, observably much higher fluorescence intensity indicates that both CO-releasing molecules increased vessel density in embryos exposed to the doses from 5 and 10  $\mu$ M,

contrary to their inhibitory effect at higher doses ( $\geq 25 \mu\text{M}$ ). This observation is in line with previously reported studies [25].

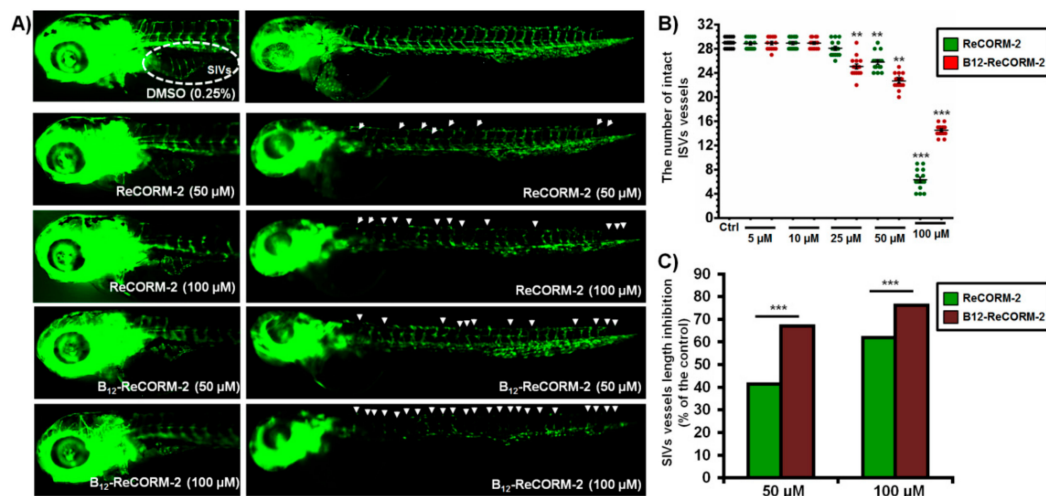


**Figure 7.** The suppression of neovascularization in developing zebrafish embryos by ReCORM-2 and B<sub>12</sub>-ReCORM-2 treatments assessed according to the ISV vessel development at 48 hpf and the SIVs vessel development at 72 hpf. Treatments' effect on the fluorescently labeled vasculature in *Tg(fli1:EGFP)* embryos was shown (A). The tested compounds achieved a dose-dependent inhibition of the ISV vessel development, compared to the ISVs number in the control group (B); the effect on the SIVs basket development was the most pronounced at the doses  $\geq 50 \mu\text{M}$  (C). \*\*  $p < 0.01$ ; \*\*\*  $p < 0.001$ .

Having established that the examined CO-releasing molecules show no toxic responses in zebrafish embryos at doses as high as  $100 \mu\text{M}$ , we finally loaded Re-CORM-2 and B<sub>12</sub>-ReCORM-2 into *Aulacoseira* frustules (13 and  $20 \mu\text{m}$  in size) and evaluated the toxicity of the drug-free micro-frustules in vivo. In these experiments, we evaluated *Aulacoseira* diatoms to address their effects on embryos' survival, development (teratogenicity), inner organs functioning, and particularly their inflammatory response. The zebrafish model has been proven particularly suitable for the toxicity assessment of nanoparticles and biomaterials [82–85]. In our experiment, embryos were in direct contact with diatoms of 13 and  $20 \mu\text{m}$  in size for a period of 114 h (from 6 to 120 hpf). The results obtained after 5-days exposure showed no evidence of any detrimental effects to the organisms at concentrations up to  $200 \mu\text{g/mL}$  (Figures 7A and 8A), indicating that the tested silicate frustules are safe. Inflammation is the most common adverse tissue reaction towards drug carrier-materials, nanoparticles, and released drugs. Since neutrophils migration, infiltration and accumulation within inflamed tissue represent the hallmark of primary host response to inflammation [86–88], we have evaluated whether the tested micro-frustules provoked an inflammatory response in zebrafish embryos after 5-days exposure. Accordingly, we used embryos of the transgenic *Tg(mpx:EGFP)* zebrafish line with fluorescently labeled neutrophils, which enabled us to visualize the neutrophils' burden, recruitment, chemotaxis, and accumulation within damaged tissues after exposure to the diatoms, as previously shown [71,89,90]. The zebrafish embryonic epithelium is very thin and consists of only two layers of epidermal cells [91]. This characteristic makes the zebrafish embryos very sensitive to exposed materials and tractable for the inflammatory response. In this study, when zebrafish embryos were exposed to various concentrations *Aulacoseira* diatoms, we observed no difference in neutrophil abundance between the control (untreated) and diatoms-exposed group (Figure 8B). Moreover, we did not observe neutrophils chemotaxis and accumulation at any particular site (organ) of the body, suggesting that silicate frustules did not induce any inflammatory response in the embryos within the timeframe of exposure. Such frustules can, thus, be regarded as safe within the tested dose range.

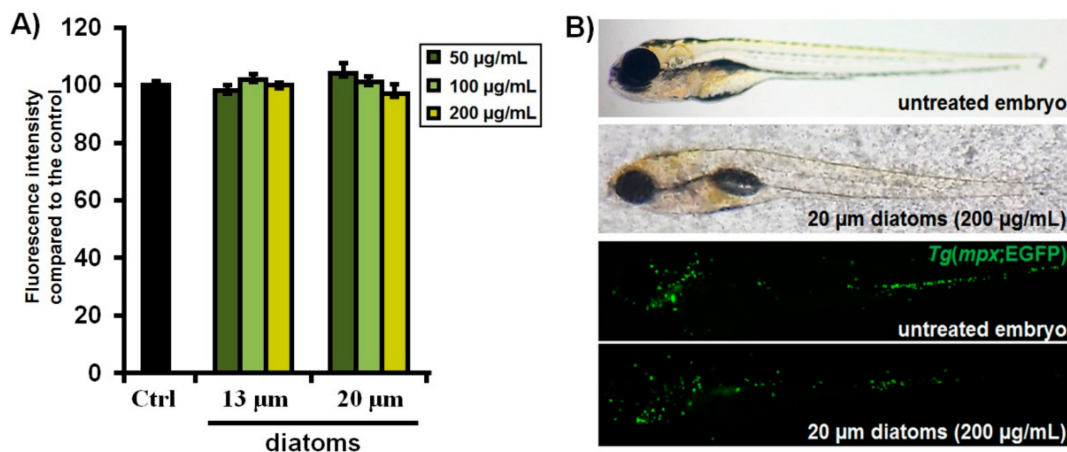


**Figure 8.** Inflammatory response in *Tg(mpx:EGFP)* embryos after the 114-h exposure to the silicate diatoms (13 and 20 µm in size). Fluorescence intensity of EGFP-labelled neutrophils (A) and morphology and neutrophils occurrence within the body of the exposed embryos (B) are shown.

#### 4. Conclusions

In conclusion, we showed via FT-IR spectromicroscopy imaging that Re-based CORMs can be chemisorbed on diatom frustules without affecting their CO-releasing properties and that the same rapidly discharged the molecules in PBS buffer. Both CORMs showed a concentration-dependent effect on the neovascularization in developing zebrafish. Angiogenesis stimulation was observed at lower drug doses (<25 µM) while angiogenesis inhibition at the higher doses. B<sub>12</sub>-ReCORM-2 revealed more profound effects than ReCORM-2. Neither the CORMs, nor the diatom carriers, showed any sign of toxicity in vivo at very high doses. In particular, the materials stimulated no inflammatory reaction as the major tissue response to the exogenous administration. Both of these properties could be beneficial for their potential therapeutic application, e.g., the stimulation of wound healing (expected to occur upon lower doses) or the anticancer effect (expected at higher doses). In the future, we plan to evaluate the effects of the molecules and loaded diatoms on doxorubicin-induced cardiac cell death.

**Supplementary Materials:** The following are available online at <http://www.mdpi.com/2076-3417/10/20/7380/s1>, Figure S1: The suppression of neovascularization in developing zebrafish embryos by ReCORM-2 and B<sub>12</sub>-ReCORM-2 treatments assessed according to the ISV vessels development at 48 hpf. Suppressed ISVs angiogenesis was indicated by red dashed arrows, while white arrow indicates the vessels in the hematopoietic tissue that increased fluorescence compared to the control ones seemed to be stimulated, Table S1: Lethal and teratogenic effects observed in zebrafish (*Danio rerio*) embryos at different hours post-fertilization (hpf).

**Author Contributions:** Conceptualization, A.P. and F.Z.; methodology, J.D. and N.R.; software, all authors; validation, A.P. and F.Z.; formal analysis, all authors; investigation, all authors; resources, A.P. and F.Z.; data curation, J.D. and N.R.; writing—original draft preparation, J.D. and N.R.; writing—review and editing, A.P. and F.Z.; supervision, A.P. and F.Z.; project administration, A.P. and F.Z.; funding acquisition, A.P. and F.Z. All authors have read and agreed to the published version of the manuscript.

**Funding:** Financial support from the Swiss National Science Foundation (Grant# PP00P2\_170589 to J.D. and F.Z.), the Canton of Fribourg (1259-0001 to J.D.), and the Institute of Molecular Genetics and Genetic Engineering from the University of Belgrade (Ministry of Education, Science and Technological Development of the Republic of Serbia, Project No.173048 (to N.R. and A.P.) are gratefully acknowledged.

**Conflicts of Interest:** The authors declare no conflict of interest. The funders had no role in the design of the study; in the collection, analyses, or interpretation of data; in the writing of the manuscript, or in the decision to publish the results.

## References

1. Davidge, K.S.; Motterlini, R.; Mann, B.E.; Wilson, J.L.; Poole, R.K. Carbon Monoxide in Biology and Microbiology: Surprising Roles for the “Detroit Perfume”. In *Advances in Microbial Physiology*; Poole, R.K., Ed.; Academic Press: Cambridge, UK, 2009; Volume 56, pp. 85–167.
2. Motterlini, R.; Otterbein, L.E. The therapeutic potential of carbon monoxide. *Nat. Rev. Drug Discov.* **2010**, *9*, 728–743. [[CrossRef](#)]
3. Heinemann, S.H.; Hoshi, T.; Westerhausen, M.; Schiller, A. Carbon monoxide—Physiology, detection and controlled release. *Chem. Commun.* **2014**, *50*, 3644–3660. [[CrossRef](#)]
4. Gullotta, F.; Masi, A.D.; Ascenzi, P. Carbon monoxide: An unusual drug. *IUBMB Life* **2012**, *64*, 378–386. [[CrossRef](#)] [[PubMed](#)]
5. Chatterjee, P.K. Physiological activities of carbon monoxide-releasing molecules: Ça ira. *Br. J. Pharmacol.* **2007**, *150*, 961–962. [[CrossRef](#)] [[PubMed](#)]
6. Prieto, L.; Rossier, J.; Derszniak, K.; Dybas, J.; Oetterli, R.M.; Kottelat, E.; Chlopicki, S.; Zelder, F.; Zobi, F. Modified biovectors for the tuneable activation of anti-platelet carbon monoxide release. *Chem. Commun.* **2017**, *53*, 6840–6843. [[CrossRef](#)] [[PubMed](#)]
7. Tranter, M.; Jones, W.K. Anti-inflammatory effects of HO-1 activity in vascular endothelial cells, commentary on “Carbon monoxide donors or heme oxygenase (HO-1) overexpression blocks interleukin-18-mediated NF- $\kappa$ B–PTEN-dependent human cardiac endothelial cell death”. *Free Radic. Biol. Med.* **2008**, *44*, 261–263. [[CrossRef](#)] [[PubMed](#)]
8. Foresti, R.; Bani-Hani, M.G.; Motterlini, R. Use of carbon monoxide as a therapeutic agent: Promises and challenges. *Intensive Care Med.* **2008**, *34*, 649–658. [[CrossRef](#)] [[PubMed](#)]
9. Sun, B.W.; Chen, X. Carbon monoxide releasing molecules: New insights for anticoagulation strategy in sepsis. *Cell. Mol. Life Sci.* **2008**, *66*, 365. [[CrossRef](#)] [[PubMed](#)]
10. Schatzschneider, U. Novel lead structures and activation mechanisms for CO-releasing molecules (CORMs). *Br. J. Pharmacol.* **2015**, *172*, 1638–1650. [[CrossRef](#)]
11. Upadhyay, K.K.; Jadeja, R.N.; Vyas, H.S.; Pandya, B.; Joshi, A.; Vohra, A.; Thounaojam, M.C.; Martin, P.M.; Bartoli, M.; Devkar, R.V. Carbon monoxide releasing molecule-A1 improves nonalcoholic steatohepatitis via Nrf2 activation mediated improvement in oxidative stress and mitochondrial function. *Redox Biol.* **2020**, *28*, 101314. [[CrossRef](#)]
12. Choi, Y.K.; Park, J.H.; Baek, Y.-Y.; Won, M.-H.; Jeoung, D.; Lee, H.; Ha, K.-S.; Kwon, Y.-G.; Kim, Y.-M. Carbon monoxide stimulates astrocytic mitochondrial biogenesis via L-type Ca<sup>2+</sup> channel-mediated PGC-1 $\alpha$ /ERR $\alpha$  activation. *Biochem. Biophys. Res. Commun.* **2016**, *479*, 297–304. [[CrossRef](#)]
13. Suliman, H.B.; Zobi, F.; Piantadosi, C.A. Heme Oxygenase-1/Carbon Monoxide System and Embryonic Stem Cell Differentiation and Maturation into Cardiomyocytes. *Antiox. Redox Sign.* **2016**, *24*, 345–360. [[CrossRef](#)] [[PubMed](#)]
14. Lancel, S.; Montaigne, D.; Marechal, X.; Marciniak, C.; Hassoun, S.M.; Decoster, B.; Ballot, C.; Blazejewski, C.; Corseaux, D.; Lescure, B.; et al. Carbon monoxide improves cardiac function and mitochondrial population quality in a mouse model of metabolic syndrome. *PLoS ONE* **2012**, *7*, e41836. [[CrossRef](#)]
15. Lancel, S.; Hassoun, S.M.; Favory, R.; Decoster, B.; Motterlini, R.; Neviere, R. Carbon Monoxide Rescues Mice from Lethal Sepsis by Supporting Mitochondrial Energetic Metabolism and Activating Mitochondrial Biogenesis. *J. Pharmacol. Exp. Ther.* **2009**, *329*, 641–648. [[CrossRef](#)]
16. Soni, H.; Pandya, G.; Patel, P.; Acharya, A.; Jain, M.; Mehta, A.A. Beneficial effects of carbon monoxide-releasing molecule-2 (CORM-2) on acute doxorubicin cardiotoxicity in mice: Role of oxidative stress and apoptosis. *Toxicol. Appl. Pharmacol.* **2011**, *253*, 70–80. [[CrossRef](#)]
17. Musameh, M.D.; Green, C.J.; Mann, B.E.; Motterlini, R.; Fuller, B.J. CO liberated from a carbon monoxide-releasing molecule exerts a positive inotropic effect in doxorubicin-induced cardiomyopathy. *J. Cardiovasc. Pharmacol.* **2010**, *55*, 168–175. [[CrossRef](#)] [[PubMed](#)]
18. Kourtis, M.; Jiang, W.G.; Cai, J. Aspects of Carbon Monoxide in Form of CO-Releasing Molecules Used in Cancer Treatment: More Light on the Way. *Oxid. Med. Cell. Longev.* **2017**, *2017*, 9326454. [[CrossRef](#)] [[PubMed](#)]
19. Fayad-Kobeissi, S.; Ratovonantenaina, J.; Dabiré, H.; Wilson, J.L.; Rodriguez, A.M.; Berdeaux, A.; Dubois-Randé, J.-L.; Mann, B.E.; Motterlini, R.; Foresti, R. Vascular and angiogenic activities of CORM-401, an oxidant-sensitive CO-releasing molecule. *Biochem. Pharmacol.* **2016**, *102*, 64–77. [[CrossRef](#)]

20. Choi, Y.K.; Kim, C.K.; Lee, H.; Jeoung, D.; Ha, K.S.; Kwon, Y.G.; Kim, K.W.; Kim, Y.M. Carbon monoxide promotes VEGF expression by increasing HIF-1 $\alpha$  protein level via two distinct mechanisms, translational activation and stabilization of HIF-1 $\alpha$  protein. *J. Biol. Chem.* **2010**, *285*, 32116–32125. [[CrossRef](#)]
21. Segersvärd, H.; Lakkisto, P.; Hänninen, M.; Forsten, H.; Siren, J.; Immonen, K.; Kosonen, R.; Sarparanta, M.; Laine, M.; Tikkanen, I. Carbon monoxide releasing molecule improves structural and functional cardiac recovery after myocardial injury. *Eur. J. Pharmacol.* **2018**, *818*, 57–66. [[CrossRef](#)]
22. Lakkisto, P.; Kytö, V.; Forsten, H.; Siren, J.-M.; Segersvärd, H.; Voipio-Pulkki, L.-M.; Laine, M.; Pulkki, K.; Tikkanen, I. Heme oxygenase-1 and carbon monoxide promote neovascularization after myocardial infarction by modulating the expression of HIF-1 $\alpha$ , SDF-1 $\alpha$  and VEGF-B. *Eur. J. Pharmacol.* **2010**, *635*, 156–164. [[CrossRef](#)] [[PubMed](#)]
23. Jozkovicz, A.; Huk, I.; Nigisch, A.; Weigel, G.; Dietrich, W.; Motterlini, R.; Dulak, J. Heme oxygenase and angiogenic activity of endothelial cells: Stimulation by carbon monoxide and inhibition by tin protoporphyrin-IX. *Antioxid. Redox Signal.* **2003**, *5*, 155–162. [[CrossRef](#)] [[PubMed](#)]
24. Ponzetti, M.; Capulli, M.; Angelucci, A.; Ventura, L.; Monache, S.D.; Mercurio, C.; Calgani, A.; Sanità, P.; Teti, A.; Rucci, N. Non-conventional role of haemoglobin beta in breast malignancy. *Br. J. Cancer* **2017**, *117*, 994–1006. [[CrossRef](#)]
25. Szabo, C. Gasotransmitters in cancer: From pathophysiology to experimental therapy. *Nat. Rev. Drug Discov.* **2016**, *15*, 185–203. [[CrossRef](#)] [[PubMed](#)]
26. Santoro, G.; Beltrami, R.; Kottelat, E.; Blacque, O.; Bogdanova, A.Y.; Zobi, F. N-Nitrosamine-(cis-Re[CO](2))(2+) cobalamin conjugates as mixed CO/NO-releasing molecules. *Dalton Trans.* **2016**, *45*, 1504–1513. [[CrossRef](#)] [[PubMed](#)]
27. Zobi, F.; Blacque, O.; Jacobs, R.A.; Schaub, M.C.; Bogdanova, A.Y. 17 e(-) rhenium dicarbonyl CO-releasing molecules on a cobalamin scaffold for biological application. *Dalton Trans.* **2012**, *41*, 370–378. [[CrossRef](#)] [[PubMed](#)]
28. Zobi, F.; Degonda, A.; Schaub, M.C.; Bogdanova, A.Y. CO Releasing Properties and Cytoprotective Effect of cis-trans- [Re-II(CO)(2)Br2L2](n) Complexes. *Inorg. Chem.* **2010**, *49*, 7313–7322. [[CrossRef](#)]
29. Clede, S.; Lambert, F.; Saint-Fort, R.; Plamont, M.A.; Bertrand, H.; Vessieres, A.; Policar, C. Influence of the Side-Chain Length on the Cellular Uptake and the Cytotoxicity of Rhenium Triscarbonyl Derivatives: A Bimodal Infrared and Luminescence Quantitative Study. *Chem. Eur. J.* **2014**, *20*, 8714–8722. [[CrossRef](#)]
30. Hostachy, S.; Policar, C.; Delsuc, N. Re(I) carbonyl complexes: Multimodal platforms for inorganic chemical biology. *Coord. Chem. Rev.* **2017**, *351*, 172–188. [[CrossRef](#)]
31. Quaroni, L.; Obst, M.; Nowak, M.; Zobi, F. Three-Dimensional Mid-Infrared Tomographic Imaging of Endogenous and Exogenous Molecules in a Single Intact Cell with Subcellular Resolution. *Angew. Chem. Int. Ed.* **2015**, *54*, 318–322. [[CrossRef](#)]
32. Santoro, G.; Zlateva, T.; Ruggi, A.; Quaroni, L.; Zobi, F. Synthesis, characterization and cellular location of cytotoxic constitutional organometallic isomers of rhenium delivered on a cyanocobalmin scaffold. *Dalton Trans.* **2015**, *44*, 6999–7008. [[CrossRef](#)] [[PubMed](#)]
33. Zobi, F.; Quaroni, L.; Santoro, G.; Zlateva, T.; Blacque, O.; Sarafimov, B.; Schaub, M.C.; Bogdanova, A.Y. Live-Fibroblast IR Imaging of a Cytoprotective PhotoCORM Activated with Visible Light. *J. Med. Chem.* **2013**, *56*, 6719–6731. [[CrossRef](#)] [[PubMed](#)]
34. Lam, Z.; Kong, K.V.; Olivo, M.; Leong, W.K. Vibrational spectroscopy of metal carbonyls for bio-imaging and -sensing. *Analyst* **2016**, *141*, 1569–1586. [[CrossRef](#)] [[PubMed](#)]
35. Clede, S.; Lambert, F.; Sandt, C.; Gueroui, Z.; Refregiers, M.; Plamont, M.A.; Dumas, P.; Vessieres, A.; Policar, C. A rhenium tris-carbonyl derivative as a single core multimodal probe for imaging (SCoMPI) combining infrared and luminescent properties. *Chem. Commun.* **2012**, *48*, 7729–7731. [[CrossRef](#)] [[PubMed](#)]
36. Clede, S.; Lambert, F.; Sandt, C.; Gueroui, Z.; Delsuc, N.; Dumas, P.; Vessieres, A.; Policar, C. Synchrotron radiation FTIR detection of a metal-carbonyl tamoxifen analog. Correlation with luminescence microscopy to study its subcellular distribution. *Biotechnol. Adv.* **2013**, *31*, 393–395. [[CrossRef](#)] [[PubMed](#)]
37. Kong, K.V.; Chew, W.; Lim, L.H.K.; Fan, W.Y.; Leong, W.K. Bioimaging in the Mid-Infrared Using an Organometallic Carbonyl Tag. *Bioconjugate Chem.* **2007**, *18*, 1370–1374. [[CrossRef](#)]
38. Clède, S.; Lambert, F.; Sandt, C.; Kascakova, S.; Unger, M.; Harté, E.; Plamont, M.-A.; Saint-Fort, R.; Deniset-Besseau, A.; Gueroui, Z.; et al. Detection of an estrogen derivative in two breast cancer cell lines using a single core multimodal probe for imaging (SCoMPI) imaged by a panel of luminescent and vibrational techniques. *Analyst* **2013**, *138*, 5627–5638. [[CrossRef](#)]

39. Policar, C.; Waern, J.B.; Plamont, M.-A.; Clède, S.; Mayet, C.; Prazeres, R.; Ortega, J.-M.; Vessières, A.; Dazzi, A. Subcellular IR Imaging of a Metal–Carbonyl Moiety Using Photothermally Induced Resonance. *Angew. Chem. Int. Ed.* **2011**, *50*, 860–864. [[CrossRef](#)]
40. Nguyen, D.; Boyer, C. Macromolecular and Inorganic Nanomaterials Scaffolds for Carbon Monoxide Delivery: Recent Developments and Future Trends. *ACS Biomater. Sci. Eng.* **2015**, *1*, 895–913. [[CrossRef](#)]
41. Inaba, H.; Fujita, K.; Ueno, T. Design of biomaterials for intracellular delivery of carbon monoxide. *Biomater. Sci.* **2015**, *3*, 1423–1438. [[CrossRef](#)]
42. Kautz, A.C.; Kunz, P.C.; Janiak, C. CO-releasing molecule (CORM) conjugate systems. *Dalton Trans.* **2016**, *45*, 18045–18063. [[CrossRef](#)] [[PubMed](#)]
43. Hasegawa, U.; van der Vlies, A.J.; Simeoni, E.; Wandrey, C.; Hubbell, J.A. Carbon Monoxide-Releasing Micelles for Immunotherapy. *J. Am. Chem. Soc.* **2010**, *132*, 18273–18280. [[CrossRef](#)] [[PubMed](#)]
44. Cheng, J.; Zheng, B.; Cheng, S.; Zhang, G.; Hu, J. Metal-free carbon monoxide-releasing micelles undergo tandem photochemical reactions for cutaneous wound healing. *Chem. Sci.* **2020**, *11*, 4499–4507. [[CrossRef](#)]
45. Kunz, P.C.; Meyer, H.; Barthel, J.; Sollazzo, S.; Schmidt, A.M.; Janiak, C. Metal carbonyls supported on iron oxide nanoparticles to trigger the CO-gasotransmitter release by magnetic heating. *Chem. Commun.* **2013**, *49*, 4896–4898. [[CrossRef](#)]
46. Ma, M.; Noei, H.; Mienert, B.; Niesel, J.; Bill, E.; Muhler, M.; Fischer, R.A.; Wang, Y.; Schatzschneider, U.; Metzler-Nolte, N. Iron Metal–Organic Frameworks MIL-88B and NH<sub>2</sub>-MIL-88B for the Loading and Delivery of the Gasotransmitter Carbon Monoxide. *Chem. Eur. J.* **2013**, *19*, 6785–6790. [[CrossRef](#)]
47. Nguyen, D.; Nguyen, T.-K.; Rice, S.A.; Boyer, C. CO-Releasing Polymers Exert Antimicrobial Activity. *Biomacromolecules* **2015**, *16*, 2776–2786. [[CrossRef](#)]
48. Bohlender, C.; Wolfram, M.; Goerls, H.; Imhof, W.; Menzel, R.; Baumgaertel, A.; Schubert, U.S.; Mueller, U.; Frigge, M.; Schnabelrauch, M.; et al. Light-triggered NO release from a nanofibrous non-woven. *J. Mater. Chem.* **2012**, *22*, 8785–8792. [[CrossRef](#)]
49. Bohlender, C.; Gläser, S.; Klein, M.; Weisser, J.; Thein, S.; Neugebauer, U.; Popp, J.; Wyrwa, R.; Schiller, A. Light-triggered CO release from nanoporous non-wovens. *J. Mater. Chem. B* **2014**, *2*, 1454–1463. [[CrossRef](#)]
50. Carmona, F.J.; Jiménez-Amezcuca, I.; Rojas, S.; Romão, C.C.; Navarro, J.A.R.; Maldonado, C.R.; Barea, E. Aluminum Doped MCM-41 Nanoparticles as Platforms for the Dual Encapsulation of a CO-Releasing Molecule and Cisplatin. *Inorg. Chem.* **2017**, *56*, 10474–10480. [[CrossRef](#)]
51. Bohlender, C.; Landfester, K.; Crespy, D.; Schiller, A. Unconventional Non-Aqueous Emulsions for the Encapsulation of a Phototriggerable NO-Donor Complex in Polymer Nanoparticles. *Part. Part. Syst. Charact.* **2013**, *30*, 138–142. [[CrossRef](#)]
52. Dördelmann, G.; Meinhardt, T.; Sowik, T.; Krueger, A.; Schatzschneider, U. CuAAC click functionalization of azide-modified nanodiamond with a photoactivatable CO-releasing molecule (PhotoCORM) based on [Mn(CO)<sub>3</sub>(tpm)]<sup>+</sup>. *Chem. Commun.* **2012**, *48*, 11528–11530. [[CrossRef](#)] [[PubMed](#)]
53. Dördelmann, G.; Pfeiffer, H.; Birkner, A.; Schatzschneider, U. Silicon Dioxide Nanoparticles As Carriers for Photoactivatable CO-Releasing Molecules (PhotoCORMs). *Inorg. Chem.* **2011**, *50*, 4362–4367. [[CrossRef](#)]
54. Morse, D.E. Silicon biotechnology: Harnessing biological silica production to construct new materials. *Trends Biotechnol.* **1999**, *17*, 230–232. [[CrossRef](#)]
55. Delasoie, J.; Zobi, F. Natural Diatom Biosilica as Microshuttles in Drug Delivery Systems. *Pharmaceutics* **2019**, *11*, 537. [[CrossRef](#)]
56. Terracciano, M.; De Stefano, L.; Rea, I. Diatoms Green Nanotechnology for Biosilica-Based Drug Delivery Systems. *Pharmaceutics* **2018**, *10*, 242. [[CrossRef](#)] [[PubMed](#)]
57. Uthappa, U.T.; Brahmkhatri, V.; Sriram, G.; Jung, H.-Y.; Yu, J.; Kurkuri, N.; Aminabhavi, T.M.; Altalhi, T.; Neelgund, G.M.; Kurkuri, M.D. Nature engineered diatom biosilica as drug delivery systems. *J. Control. Release* **2018**, *281*, 70–83. [[CrossRef](#)]
58. Wang, Y.; Cai, J.; Jiang, Y.; Jiang, X.; Zhang, D. Preparation of biosilica structures from frustules of diatoms and their applications: Current state and perspectives. *Appl. Microbiol. Biotechnol.* **2013**, *97*, 453–460. [[CrossRef](#)] [[PubMed](#)]
59. Tramontano, C.; Chianese, G.; Terracciano, M.; Napolitano, M.; De Stefano, L.; Rea, I. Nanostructured Biosilica of Diatoms: From Water World to Biomedical Applications. *Appl. Sci.* **2020**, *10*, 6811. [[CrossRef](#)]
60. Rea, I.; Terracciano, M.; De Stefano, L. Synthetic vs Natural: Diatoms Bioderived Porous Materials for the Next Generation of Healthcare Nanodevices. *Adv. Healthc. Mater.* **2017**, *6*, 1601125. [[CrossRef](#)]

61. Zobi, F.; Kromer, L.; Spingler, B.; Alberto, R. Synthesis and Reactivity of the 17 e<sup>-</sup> Complex [(ReBr<sub>4</sub>)-Br-II(CO)(2)](2-): A Convenient Entry into Rhenium(II) Chemistry. *Inorg. Chem.* **2009**, *48*, 8965–8970. [[CrossRef](#)]
62. Delasoie, J.; Rossier, J.; Haeni, L.; Rothen-Rutishauser, B.; Zobi, F. Slow-targeted release of a ruthenium anticancer agent from vitamin B-12 functionalized marine diatom microalgae. *Dalton Trans.* **2018**, *47*, 17221–17232. [[CrossRef](#)]
63. Vasani, R.B.; Losic, D.; Cavallaro, A.; Voelcker, N.H. Fabrication of stimulus-responsive diatom biosilica microcapsules for antibiotic drug delivery. *J. Mater. Chem. B* **2015**, *3*, 4325–4329. [[CrossRef](#)] [[PubMed](#)]
64. Delasoie, J.; Schiel, P.; Vojnovic, S.; Nikodinovic-Runic, J.; Zobi, F. Photoactivatable Surface-Functionalized Diatom Microalgae for Colorectal Cancer Targeted Delivery and Enhanced Cytotoxicity of Anticancer Complexes. *Pharmaceutics* **2020**, *12*, 480. [[CrossRef](#)] [[PubMed](#)]
65. Zhang, H.; Shahbazi, M.A.; Makila, E.M.; da Silva, T.H.; Reis, R.L.; Salonen, J.J.; Hirvonen, J.T.; Santos, H.A. Diatom silica microparticles for sustained release and permeation enhancement following oral delivery of prednisone and mesalazine. *Biomaterials* **2013**, *34*, 9210–9219. [[CrossRef](#)] [[PubMed](#)]
66. Aw, M.S.; Bariana, M.; Yu, Y.; Addai-Mensah, J.; Losic, D. Surface-functionalized diatom microcapsules for drug delivery of water-insoluble drugs. *J. Biomat. Appl.* **2013**, *28*, 163–174. [[CrossRef](#)]
67. Motterlini, R.; Sawle, P.; Bains, S.; Hammad, J.; Alberto, R.; Foresti, R.; Green, C.J. CORM-A1: A new pharmacologically active carbon monoxide-releasing molecule. *FASEB J.* **2005**, *19*, 1–24. [[CrossRef](#)]
68. Sovari, S.N.; Vojnovic, S.; Bogojevic, S.S.; Crochet, A.; Pavic, A.; Nikodinovic-Runic, J.; Zobi, F. Design, synthesis and in vivo evaluation of 3-arylcoumarin derivatives of rhenium(I) tricarbonyl complexes as potent antibacterial agents against methicillin-resistant *Staphylococcus aureus* (MRSA). *Eur. J. Med. Chem.* **2020**, *205*, 112533. [[CrossRef](#)]
69. Delasoie, J.; Pavic, A.; Voutier, N.; Vojnovic, S.; Crochet, A.; Nikodinovic-Runic, J.; Zobi, F. Identification of novel potent and non-toxic anticancer, anti-angiogenic and antimetastatic rhenium complexes against colorectal carcinoma. *Eur. J. Med. Chem.* **2020**, *204*, 112583. [[CrossRef](#)]
70. Renshaw, S.A.; Loynes, C.A.; Trushell, D.M.I.; Elworthy, S.; Ingham, P.W.; Whyte, M.K.B. A transgenic zebrafish model of neutrophilic inflammation. *Blood* **2006**, *108*, 3976–3978. [[CrossRef](#)]
71. Duan, J.; Liang, S.; Yu, Y.; Li, Y.; Wang, L.; Wu, Z.; Chen, Y.; Miller, M.R.; Sun, Z. Inflammation–coagulation response and thrombotic effects induced by silica nanoparticles in zebrafish embryos. *Nanotoxicology* **2018**, *12*, 470–484. [[CrossRef](#)]
72. Warring, S.L.; Beattie, D.A.; McQuillan, A.J. Surficial Siloxane-to-Silanol Interconversion during Room-Temperature Hydration/Dehydration of Amorphous Silica Films Observed by ATR-IR and TIR-Raman Spectroscopy. *Langmuir* **2016**, *32*, 1568–1576. [[CrossRef](#)] [[PubMed](#)]
73. Zobi, F. Parametrization of the Contribution of Mono- and Bidentate Ligands on the Symmetric C O Stretching Frequency of fac-[Re(CO)(3)](+) Complexes. *Inorg. Chem.* **2009**, *48*, 10845–10855. [[CrossRef](#)] [[PubMed](#)]
74. Zobi, F. Ligand Electronic Parameters as a Measure of the Polarization of the C O Bond in [M(CO)(x)L-y](n) Complexes and of the Relative Stabilization of [M(CO)(x)L-y](n/n+1) Species. *Inorg. Chem.* **2010**, *49*, 10370–10377. [[CrossRef](#)] [[PubMed](#)]
75. Zobi, F.; Blacque, O. Reactivity of 17 e<sup>-</sup> Complex [(ReBr<sub>4</sub>)-Br-II(CO)(2)](2-) with Bridging Aromatic Ligands. Characterization and CO-Releasing Properties. *Dalton Trans.* **2011**, *40*, 4994–5001. [[CrossRef](#)] [[PubMed](#)]
76. Yue, S.; Fang, D.W.; Li, J.; Zang, S.L.; Zhou, M.D.; Zhang, B.; Markovits, I.I.E.; Cokoja, M.; Kuhn, F.E. Synthesis and Characterization of Imidazolium Perrhenate Ionic Liquids. *Z. Naturforsch. B* **2013**, *68*, 598–604. [[CrossRef](#)]
77. Chakraborty, C.; Hsu, C.H.; Wen, Z.H.; Lin, C.S.; Agoramorthy, G. Zebrafish: A Complete Animal Model for In Vivo Drug Discovery and Development. *Curr. Drug Metab.* **2009**, *10*, 116–124. [[CrossRef](#)]
78. MacRae, C.A.; Peterson, R.T. Zebrafish as tools for drug discovery. *Nat. Rev. Drug Discov.* **2015**, *14*, 721. [[CrossRef](#)]
79. Song, J.E.; Si, J.; Zhou, R.; Liu, H.P.; Wang, Z.G.; Gan, L.; Gui, F.; Liu, B.; Zhang, H. Effects of Exogenous Carbon Monoxide Releasing Molecules on the Development of Zebrafish Embryos and Larvae. *Biomed. Environ. Sci.* **2016**, *29*, 453–456. [[CrossRef](#)]
80. Folkman, J. Angiogenesis in cancer, vascular, rheumatoid and other disease. *Nat. Med.* **1995**, *1*, 27–30. [[CrossRef](#)]
81. Ferrara, N.; Kerbel, R.S. Angiogenesis as a therapeutic target. *Nature* **2005**, *438*, 967–974. [[CrossRef](#)]
82. Haque, E.; Ward, A.C. Zebrafish as a Model to Evaluate Nanoparticle Toxicity. *Nanomaterials* **2018**, *8*, 561. [[CrossRef](#)]
83. Witherel, C.E.; Gurevich, D.; Collin, J.D.; Martin, P.; Spiller, K.L. Host–Biomaterial Interactions in Zebrafish. *ACS Biomater. Sci. Eng.* **2018**, *4*, 1233–1240. [[CrossRef](#)]

84. Rothenbücher, T.S.P.; Ledin, J.; Gibbs, D.; Engqvist, H.; Persson, C.; Hulsart-Billström, G. Zebrafish embryo as a replacement model for initial biocompatibility studies of biomaterials and drug delivery systems. *Acta Biomater.* **2019**, *100*, 235–243. [[CrossRef](#)] [[PubMed](#)]
85. Zhang, X.; Stockhammer, O.W.; de Boer, L.; Vischer, N.O.E.; Spaink, H.P.; Grijpma, D.W.; Zaat, S.A.J. The zebrafish embryo as a model to quantify early inflammatory cell responses to biomaterials. *J. Biomed. Mater. Res. Part A* **2017**, *105*, 2522–2532. [[CrossRef](#)]
86. Mortaz, E.; Alipoor, S.D.; Adcock, I.M.; Mumby, S.; Koenderman, L. Update on Neutrophil Function in Severe Inflammation. *Front. Immunol.* **2018**, *9*, 2171. [[CrossRef](#)]
87. Rosales, C.; Lowell, C.A.; Schnoor, M.; Uribe-Querol, E. Neutrophils: Their Role in Innate and Adaptive Immunity 2017. *J. Immunol. Res.* **2017**, *2017*, 9748345. [[CrossRef](#)] [[PubMed](#)]
88. Leliefeld, P.H.C.; Koenderman, L.; Pillay, J. How Neutrophils Shape Adaptive Immune Responses. *Front. Immunol.* **2015**, *6*, 1–9. [[CrossRef](#)]
89. Brun, N.R.; Koch, B.E.V.; Varela, M.; Peijnenburg, W.J.G.M.; Spaink, H.P.; Vijver, M.G. Nanoparticles induce dermal and intestinal innate immune system responses in zebrafish embryos. *Environ. Sci. Nano* **2018**, *5*, 904–916. [[CrossRef](#)]
90. Zhang, C.; Li, C.Y.; Jia, X.J.; Wang, K.; Tu, Y.B.; Wang, R.C.; Liu, K.C.; Lu, T.; He, C.W. In Vitro and In Vivo Anti-Inflammatory Effects of Polyphyllin VII through Downregulating MAPK and NF-kappa B Pathways. *Molecules* **2019**, *24*, 875. [[CrossRef](#)]
91. Chang, W.-J.; Hwang, P.-P. Development of zebrafish epidermis. *Birth Defects Res. C Embryo Today* **2011**, *93*, 205–214. [[CrossRef](#)]

**Publisher’s Note:** MDPI stays neutral with regard to jurisdictional claims in published maps and institutional affiliations.



© 2020 by the authors. Licensee MDPI, Basel, Switzerland. This article is an open access article distributed under the terms and conditions of the Creative Commons Attribution (CC BY) license (<http://creativecommons.org/licenses/by/4.0/>).